Resonant Spin-Transfer-Torque Nano-Oscillators

Abhishek Sharma, Ashwin A. Tulapurkar, and Bhaskaran Muralidharan
Department of Electrical Engineering, Indian Institute of Technology
Bombay, Powai, Mumbai 400076, India

(Received 30 January 2017; revised manuscript received 18 September 2017; published 14 December 2017)

Spin-transfer-torque nano-oscillators are potential candidates for replacing the traditional inductor-based voltage-controlled oscillators in modern communication devices. Typical oscillator designs are based on trilayer magnetic tunnel junctions, which have the disadvantages of low power outputs and poor conversion efficiencies. We theoretically propose using resonant spin filtering in pentalayer magnetic tunnel junctions as a possible route to alleviate these issues and present viable device designs geared toward a high microwave output power and an efficient conversion of the dc input power. We attribute these robust qualities to the resulting nontrivial spin-current profiles and the ultrahigh tunnel magnetoresistance, both of which arise from resonant spin filtering. The device designs are based on the nonequilibrium Green's-function spin-transport formalism self-consistently coupled with the stochastic Landau-Lifshitz-Gilbert-Slonczewski equation and Poisson's equation. We demonstrate that the proposed structures facilitate oscillator designs featuring a large enhancement in microwave power of around 1150% and an efficiency enhancement of over 1100% compared to typical trilayer designs. We rationalize the optimum operating regions via an analysis of the dynamic and static device resistances. We also demonstrate the robustness of our structures against device design fluctuations and elastic dephasing. This work sets the stage for pentalyer spin-transfer-torque nano-oscillator device designs that ameliorate major issues associated with typical trilayer designs.

DOI: 10.1103/PhysRevApplied.8.064014

I. INTRODUCTION

Spin-transfer-torque nano-oscillators (STNOs) are a class of nonlinear nanoscale oscillators which have attracted a lot of interest from the physics as well as the applications perspective. The interest from the physics perspective stems from the need to advance the understanding of magnetization dynamics in nonlinear systems [1–5]. From the application perspective, these devices are suitable for modern communication electronics [6–8]. STNOs have better built-in features over traditionally used voltage-controlled oscillators (VCOs), such as smaller size, lower cost, and easier integrability to silicon technology. In order to technologically replace VCOs, STNOs should be able to deliver high microwave power outputs and must possess higher conversion efficiencies with a good quality factor. There have been consistent efforts [9–11] to improve the performance of STNOs based on typical trilayer magnetic tunnel junctions (MTJs). Various proposed improvements have been centered around modifying the magnetic properties of the ferromagnet. However, they have not been able to deliver microwave power outputs in excess of 0.3 μW [11]. In this work, we propose pentalayer device designs that make use of resonant spin filtering, termed as resonant-tunneling magnetic-tunnel-junction (RTMTJ) structures, to circumvent the issues faced by typical trilayer-based STNO designs. We demonstrate that, owing to the spin-filtering physics in the proposed structures [12,13], the resulting nontrivial spin-current profiles and the high tunnel magnetoresistance (TMR) translate to a significant improvement in STNO performance.

Spin-transfer torque [14,15] involves the transfer of spin angular momentum from spin-polarized charge carriers to the magnetization of the ferromagnetic layer. Spin torque can either enhance the magnetic damping inherent in magnetic systems or can compensate for the damping processes, based on the state of the ferromagnet and the direction of the spin-polarized current. When the spin-torque magnitude is large enough to compensate for magnetic damping, an instability in the magnetization dynamics results. In MTJs, the magnetic state of the free ferromagnet can be switched either parallel or antiparallel with respect to the pinned ferromagnetic layer [see Fig. 1(a)] due to spin torque under a sufficient voltage bias. The state of the free ferromagnet can be toggled back to the initial state by applying a static magnetic field, resulting in self-sustained oscillations of the magnetization in the free ferromagnetic layer. The nature of the self-sustained oscillations is governed by the magnetization dynamics incited by the spin-current profile. These self-sustained oscillations in the magnetization translate to high-frequency electrical signals due to the magnetoresistance (MR) effect. The microwave power output thus translated is directly associated with the electrical readout (i.e., the MR) and the ratio I/I_C [4], where I is the bias current and I_C is the critical current required for magnetization switching.

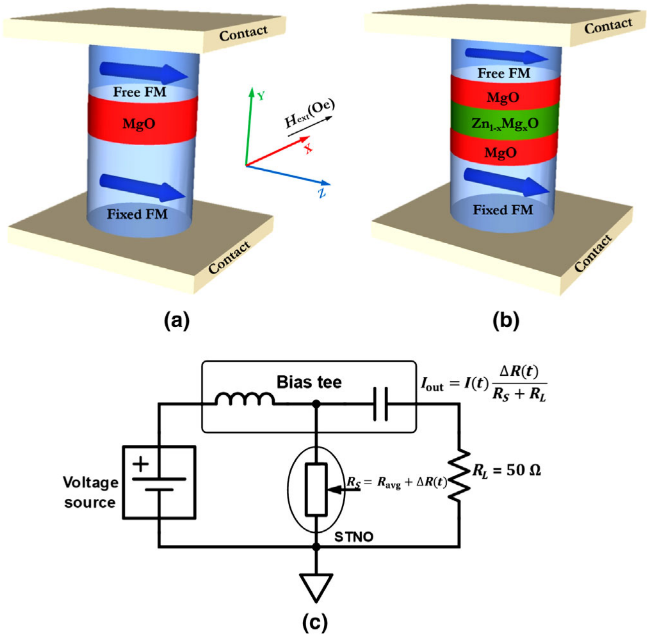

FIG. 1. Oscillator design schematics. (a) Trilayer device with an insulating MgO layer between the free and fixed ferromagnetic (FM) layers. (b) The RTMTJ-based device comprises a MgO-$Zn_{1-x}Mg_xO$-MgO heterostructure between the free and fixed ferromagnetic layers. An external-field magnetic field (H_{ext}) is applied along the $\hat{x}$ direction. (c) Circuit diagram of a STNO biased by a voltage source with the microwave power delivered to a load resistor R_L.

One may anticipate an increase in the power output by ramping up the ratio I/I_C, which can be achieved at a higher voltage bias. However, a higher bias reduces, in turn, the MR of the device, as evidenced in experiments as well as through our simulation results [see Fig. 3(b)], ultimately resulting in a reduction in the microwave output power. Therefore, high microwave power outputs through STNOs can be achieved by designing a device that combines high MR and low switching bias. Various studies have focused on lowering I_C by tailoring the magnetic properties of the ferromagnetic layer while preserving the higher MR. They have estimated that the maximum power delivered to a matched load is around 1 μW, while the maximum achieved power in experiments to date is still around 0.3 μW [11]. In this work, we thus propose harvesting the higher MR and the lower switching bias emerging from resonant spin-filtering physics [12,13,16] to increase the microwave power and the conversion efficiency of STNOs.

II. DEVICE DESIGN

Device schematics for both the trilayer and the pentalayer structures are depicted in Figs. 1(a) and 1(b), respectively. The equivalent circuit is schematized in Fig. 1(c). These designs have been simulated by employing the nonequilibrium Green's function (NEGF) [17] spin-transport formalism coupled with Poisson's equation and the Landau-Lifshitz-Gilbert-Slonczewski (LLGS) [15] equation. Details of the calculations are given in Appendix A. In this work, we also take into account the thermal noise in the form of magnetic-field fluctuations $\vec{h_r}$ in the LLGS equation with the following statistical properties [18]:

$$\langle h_{\mathrm{fl},i}(t)\rangle = 0, \langle h_{\mathrm{fl},i}h_{\mathrm{fl},j}(s)\rangle = 2D\delta_{ij}\delta(t-s), \qquad (1)$$

where i and j are Cartesian indices and $\langle\cdots\rangle$ represents the ensemble average. The strength of the fluctuation D is given by

$$D = \frac{\alpha}{1+\alpha^2}\frac{k_B T}{\gamma\mu_0 M_S V}, \qquad (2)$$

where α is the Gilbert-damping parameter, γ is the gyromagnetic ratio of the electron, μ_0 is the free-space permeability constant, k_B is the Boltzmann constant, T is the temperature of the magnetic layer, and M_S and V are the saturation magnetization and the volume of the free layer, respectively.

In the results that follow, the parameters chosen for the magnetization dynamics are $\alpha = 0.01$, the saturation magnetization $M_S = 1200\ \mathrm{emu/cm^3}$, $\gamma = 17.6$ MHz/Oe, and the anisotropy field $H_k = 75$ Oe along the $\hat{z}$ axis, which have all been extracted from Zeng *et al.* [11] after removing the zero-bias field and the demagnetization field of $H_d = 1500$ Oe [11] along the $\hat{y}$ axis. The cross-section area of all of the devices considered is $70 \times 160\ \mathrm{nm}^2$, with the thickness of the free ferromagnetic layer taken to be 1.6 nm. All of the simulations are done at room temperature. The RTMTJ structure shown in Fig. 1(b) may be realized via a heterostructure of MgO and a stoichiometrically substituted ZnO ($Zn_{1-x}Mg_xO$), whose band gap and work function may be tuned [19], particularly for the presented device design, has a stoichiometric fraction of Mg, $x = 0.43$ (see Appendix A 2).

III. RESULTS AND ANALYSIS

We show in Fig. 2(a), the current-voltage (I-V) characteristics of a trilayer device in a parallel configuration (PC) and in an antiparallel configuration (APC). The charge current is smaller in magnitude in the APC than in the PC due to spin-dependent tunneling in a trilayer device. The TMR is defined as $\mathrm{TMR} = (R_{\mathrm{AP}} - R_{\mathrm{P}})/(R_{\mathrm{P}})$, where R_{P} and R_{AP} are the resistances in the parallel and antiparallel configurations, respectively. The TMR variation with the voltage for a trilayer device is shown in Fig. 2(b). Figure 2(c) shows the variation of the Slonczewski term [20] ($I_{S\parallel}$) of the spin current (see Appendix A) with bias voltage. The Slonczewski term can either enhance the damping in the magnetization dynamics or compensate for the damping processes in the magnetic system, regulated by the direction of current. It can be seen from Fig. 2(d) that the fieldlike term [20] ($I_{S\perp}$) of the spin current is nonzero at

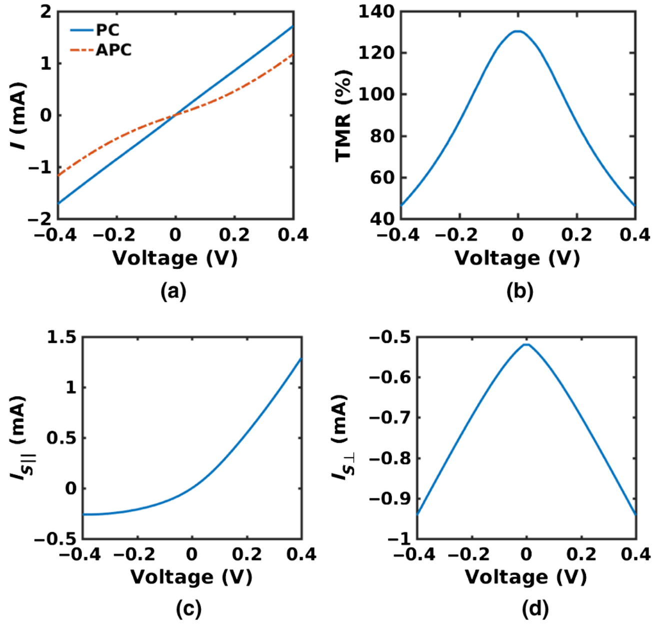

FIG. 2. Trilayer device characteristics. (a) Current variation with bias voltage in the parallel configuration (PC) and the antiparallel configuration (APC), (b) TMR variation with bias voltage, (c) $I_{S\parallel}$ (Slonczewski term), and (d) $I_{S\perp}$ (fieldlike term) variation with voltage at the perpendicular configuration of free and fixed ferromagnets.

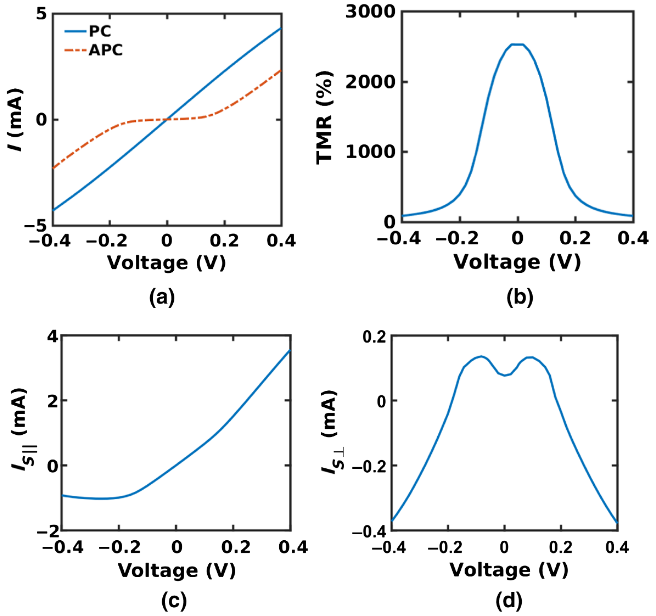

FIG. 3. Pentalayer device (RTMTJ) characteristics. (a) Current variation with bias voltage in the PC and the APC. (b) TMR variation with bias voltage. (c) $I_{S\parallel}$ (Slonczewski term). (d) $I_{S\perp}$ (fieldlike term) variation with voltage at the perpendicular configuration of free and fixed ferromagnets. We also show the angular dependence of the spin current in Appendix A 3

zero bias. This zero-bias component is a dissipationless spin current and represents the exchange coupling between the ferromagnets due to the tunnel barrier [15]. This exchange coupling can be either ferromagnetic or antiferromagnetic in nature depending upon the relative positioning of the conduction bands in the ferromagnets and the insulator. The exchange coupling is of an antiferromagnetic nature in MgO-based trilayer devices. The fieldlike term serves as the effective magnetic field in the magnetization dynamics.

The RTMTJ device has an ultrahigh TMR, as shown in Fig. 3(b), which can be tuned via appropriate positioning of the transmission peaks with respect to the Fermi level and the ferromagnetic exchange splitting Δ [13]. The resonant conduction in the PC and the off-resonant conduction in the APC [Fig. 3(a)] are responsible for the ultrahigh TMR [13]. The larger Slonczewski term $I_{S\parallel}$ in the RTMTJ device, as shown in Fig. 3(c), can be attributed to the resonant conduction and enhanced spin filtering [13]. We show in Fig. 3(d) the variation of $I_{S\perp}$ (the fieldlike term) with voltage. Here, it is interesting to note that, at zero bias, the exchange coupling is ferromagnetic in nature for the RTMTJ structure, and an applied bias tries to change this exchange coupling to antiferromagnetic. Thus, at some applied bias it is possible to decimate the exchange coupling in the RTMTJ structure.

In the case of STNOs, the nonlinearity parameters can be varied over a wide range by changing the orientation and magnitude of the applied magnetic field [4]. When the orientation and magnitude of the external field in the plane of magnetization [see Fig. 1(a)] is varied, we notice that the external magnetic field perpendicular to the easy axis leads to high microwave power outputs and narrow linewidths, consistent with the results in an earlier theoretical work [4].

Based on the circuit diagram shown in Fig. 1(c), we model the STNO as a source of time-varying resistance connected with a 50-Ω load resistance. The power delivered to the load resistance constitutes the useful microwave power that can be extracted from the STNO and is given by

$$P_{\mathrm{ac}} = R_L \mathrm{Var}\left(\frac{R_S(t) I_S(t)}{R_S(t) + R_L}\right), \tag{3}$$

where $R_L = 50\ \Omega$ and $R_S(t) = V/I_S(t)$ is the source resistance and "Var" is the variance of the time-dependent term. We show in Fig. 4(a) the microwave power as a function of voltage in the trilayer device when an in-plane field is applied perpendicular to the easy axis of the free ferromagnetic layer. It is noted that the microwave power increases with applied bias due to the large spin current [Fig. 2(c)], which results in large amplitude peak-to-peak magnetization dynamics translating to a large microwave power output. However, with a further increase in bias voltage, the microwave power starts to fall off due to the reduction in the TMR at higher voltages [Fig. 2(b)]. We show in Fig. 4(b) the variation of central frequency (f_C) of

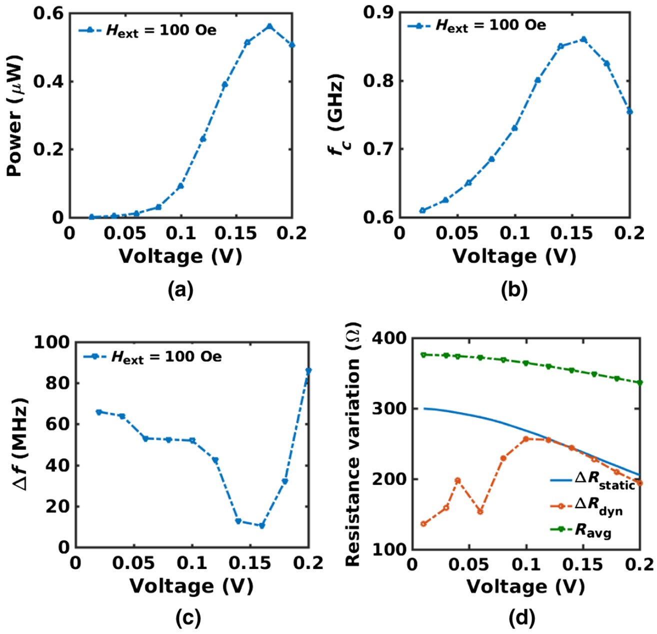

FIG. 4. Voltage-induced precession of the trilayer-MTJ device. (a) Voltage dependence of microwave power delivered to the 50-Ω load. (b) Peak frequency. (c) Full width at half maximum (FWHM) Δf. (d) Resistance variation ($\Delta R_{\mathrm{static}}$, $\Delta R_{\mathrm{dynamic}}$, R_{avg}) as a function of the bias voltage.

microwave oscillations with bias for a trilayer device. These trends in the power output and f_C can be understood by analyzing how the dynamic resistance ($\Delta R_{\mathrm{dynamic}}$), the static resistance ($\Delta R_{\mathrm{static}}$) and the average resistance (R_{avg}) vary with voltage, as shown in Fig. 4(d). The dynamic resistance is the maximum change in the resistance of the device as the current oscillates, i.e., $\Delta R_{\mathrm{dynamic}} = V/I_{\mathrm{min}} - V/I_{\mathrm{max}}$ [21]. The static resistance is the change in the resistance due to the MR effect, i.e., $\Delta R_{\mathrm{static}} = R_{\mathrm{AP}}(V) - R_{\mathrm{P}}(V)$ [21]. With an increase in bias, $\Delta R_{\mathrm{dynamic}}$ approaches $\Delta R_{\mathrm{static}}$, as can be seen in Fig. 4(d), signifying large peak-to-peak magnetization dynamics and out-of-plane oscillations of the free ferromagnetic layer [21] (see Fig. 15). The point of peak microwave power [Fig. 4(a)] is shifted by a small amount from the point where $\Delta R_{\mathrm{dynamic}}$ approaches $\Delta R_{\mathrm{static}}$ due to the loading effect of R_L. As the microwave power delivered to the load increases when the load and the source have the same resistances, any reduction in R_{avg} increases the microwave power. However, with a further increase in the bias, $\Delta R_{\mathrm{dynamic}}$ starts to deviate from $\Delta R_{\mathrm{static}}$, as seen in Fig. 4, resulting in a reduction of microwave output power. It can be seen that the central frequency [Fig. 4(b)] also peaks at around the same voltage point where $\Delta R_{\mathrm{dynamic}}$ approaches $\Delta R_{\mathrm{static}}$. The frequency of oscillations (f_C) is determined by the demagnetization field with $f_C \propto m_y$, where m_y is the out-of-plane component of the magnetization unit vector. Therefore, f_C increases as $\Delta R_{\mathrm{dynamic}}$ approaches $\Delta R_{\mathrm{static}}$, associated with a higher component of the out-of-plane magnetization (see Fig. 15). As the bias is further increased, the reduction in $\Delta R_{\mathrm{dynamic}}$ is more in comparison to $\Delta R_{\mathrm{static}}$, resulting in a smaller out-of-plane magnetization component which additionally causes the central frequency to fall at a higher voltage. Figure 4(c) shows the linewidth of the microwave signal as a function of bias voltage for the trilayer device. It is observed that the linewidth falls to 11 MHz at $V = 0.16$, delivering 0.51 μW power to the 50-Ω load at a central frequency of 860 MHz.

The microwave power for the RTMTJ-based oscillator follows a similar trend as a trilayer-based oscillator, as can be seen in Fig. 5(a). The frequency of oscillations is higher in the RTMTJ-based oscillator due to the larger spin currents [see Fig. 5(b)] compared to the trilayer device. The linewidth is also larger in this device, as shown in Fig. 5(c), but has nearly the same quality factor as that of the trilayer device. The central frequency for the RTMTJ device increases monotonically with voltage as $\Delta R_{\mathrm{dynamic}}$ steadily approaches $\Delta R_{\mathrm{static}}$ [Fig. 5(d)], making the device more suitable for the high-frequency applications.

Furthermore, it can be seen from Fig. 6(a) that the microwave power delivered to the load by the trilayer device has two operating regimes, designated as the “usual regime” and the “high-power regime.” The maximum power delivered to the load in the usual regime is around 0.5 μW. In the high-power regime, the microwave output power is nearly 1 μW under a bias of $V = 0.34$ and an external field of $H_{\mathrm{ext}} = 605$ Oe. The conversion efficiency,

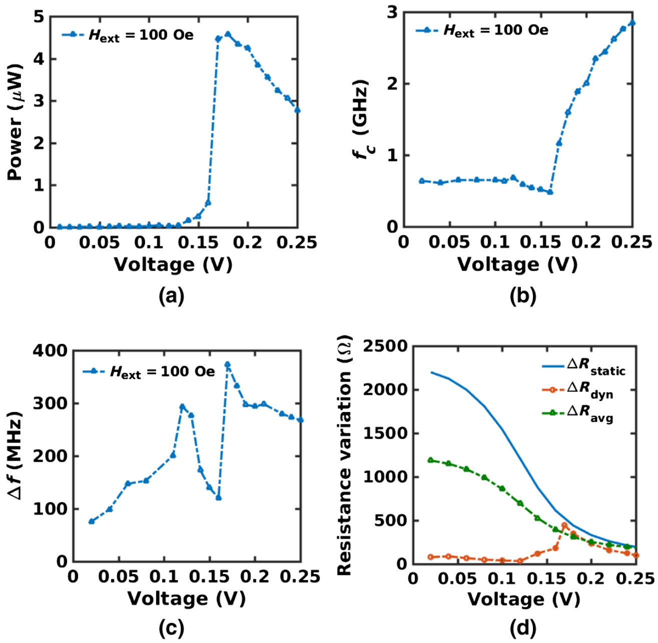

FIG. 5. Voltage-induced precession of the RTMTJ device. (a) Voltage dependence of microwave power delivered to the 50-Ω load. (b) Peak frequency. (c) FWHM Δf. (d) Resistance variation ($\Delta R_{\mathrm{static}}$, $\Delta R_{\mathrm{dynamic}}$, R_{avg}) as a function of the applied bias voltage.

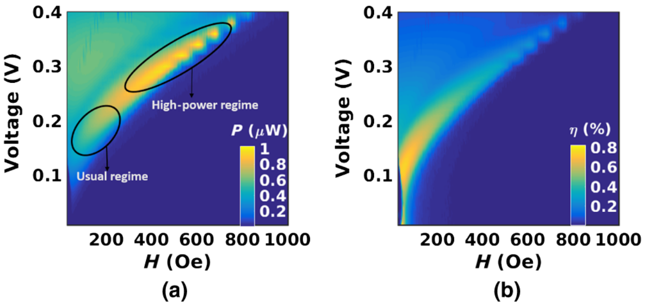

FIG. 6. Voltage-field diagram of the trilayer-MTJ device for (a) microwave power delivered to a 50-Ω load and (b) conversion efficiency η (%).

i.e., $\eta = P_{\mathrm{ac}}/P_{\mathrm{input}}$, of the trilayer-based oscillator at the maximum microwave output power point is 0.23%. The high power outputs in this regime can be associated with comparable dynamic and static resistances ($\Delta R_{\mathrm{dynamic}} = 132\ \Omega$, $\Delta R_{\mathrm{static}} = 132.1\ \Omega$), along with a small average resistance ($R_{\mathrm{avg}} = 299\ \Omega$). Because of the high spin current in the high-power regime, the frequency of oscillations is higher than in the usual regime. At the maximum power point in the high-power regime, the frequency of oscillations is $f_C = 2.45$ GHz. It can seen from Fig. 6(b) that the efficiency of a trilayer-based oscillator is higher in the usual regime than in the high-power regime due to the small input voltage bias.

Figure 7(a) shows the microwave power delivered to the 50-Ω load by a RTMTJ-based oscillator. The RTMTJ-based oscillator has two major features—namely, the high output power [see Fig. 7(a)] and the ultrahigh conversion efficiency [see Fig. 7(b)]—compared to the trilayer-based oscillator device [see Figs. 6(a) and 6(b)]. The power regime with large efficiency for the RTMTJ-based oscillator lies between $0.16 < \mathrm{voltage(V)} < 0.32$ and field of $60 < H(\mathrm{Oe}) < 400$. The maximum power delivered in the high-efficiency power regime to the 50-Ω load is 6.33 μW, which occurs at $V = 0.02$ V and an external field $H_{\mathrm{ext}} = 390$ Oe. The efficiency of the RTMTJ device at maximum power is 2.82%. Hence, the RTMTJ-based oscillator delivers nearly 500% higher power and is 1100% more efficient than the trilayer-based oscillator operating in the high-power regime. Furthermore, the RTMTJ-based device oscillator delivers nearly 1150% more power than the trilayer device operating in the usual regime.

A. Robustness of the design

We now evaluate the robustness of the RTMTJ-based oscillator by considering a small fluctuation in the width of the middle layer (the quantum well) of the heterostructure and including the effect of dephasing. First, we will discuss the effect of the thickness fluctuation on the STNO performance. The superior functionality of the RTMTJ device as a STNO relies on an ultrahigh TMR and the large spin current, which in turn depends on the appropriate positioning of the transmission peak [13]. The transmission-peak position in the pentalayer structure is highly sensitive to the quantum-well-region thickness. The RTMTJ design which we have analyzed has a well region 1 nm thick (Appendix A 2). We show in Fig. 8(a) the power spectrum for a STNO based on a RTMTJ having a 0.9-nm quantum-well thickness. The reduction in the well thickness reduces the TMR of the device from 2500% to 1800%, which in turn decreases the microwave power output. One the other hand, for a well thickness of 1.2 nm, the microwave output power, as shown in Fig. 8(a), increases up to 8 μW due to an enhancement in the TMR (3300%). It is worth noting here that the thickness fluctuation of the well region does not drastically change the TMR and the spin current due to the feedback or restoring effect of Poisson charging in the middle region of the RTMTJ structure. The RTMTJ structure with a semiconductor layer [22] as a quantum well are robust to thickness fluctuations relative to a RTMTJ with a normal metal as the middle layer [23,24]. The restoring effect of the Poisson charging makes the design of the RTMTJ-based STNOs robust to small fluctuations in the width of the middle region.

We show in Fig. 9 the effect of elastic dephasing, which includes momentum and phase relaxation on the power spectrum of the RTMTJ-based oscillators. Elastic dephasing in the system can arise via scattering due to the ionized

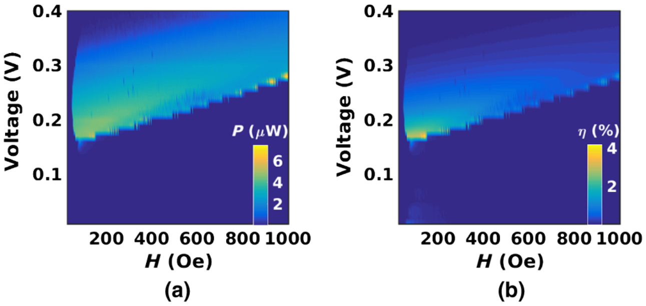

FIG. 7. Voltage-field diagram of the RTMTJ device for (a) microwave power delivered to a 50-Ω load and (b) a conversion efficiency η (%).

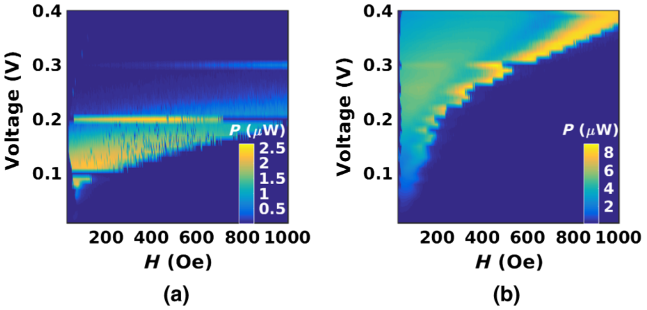

FIG. 8. Voltage-field diagram of the RTMTJ devices, with the microwave power delivered to a 50-Ω load by RTMTJs having the well widths (a) 0.9 nm and (b) 1.2 nm.

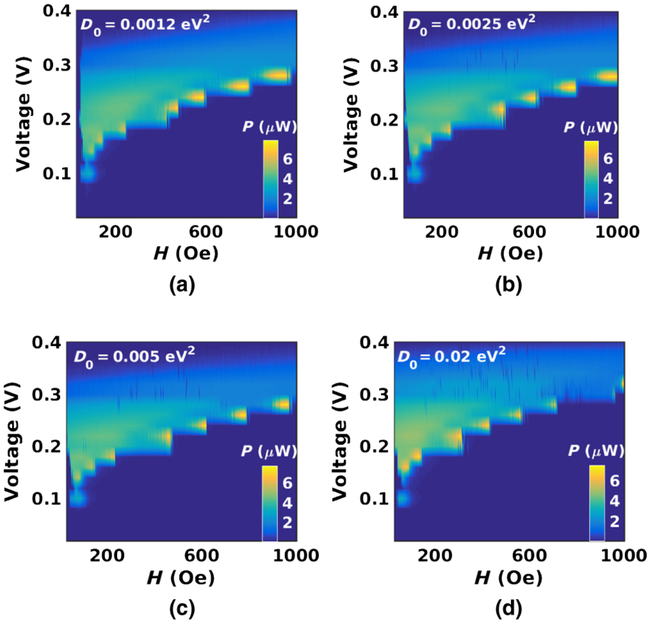

FIG. 9. Effect of elastic dephasing on a voltage-field diagram of the RTMTJ devices, with the microwave power delivered to a 50-Ω load by RTMTJ-based STNOs with the dephasing strengths (a) $D_0 = 0.0012$ eV^2, (b) $D_0 = 0.0025$ eV^2, (c) $D_0 = 0.005$ eV^2, and (d) $D_0 = 0.02$ eV^2.

impurities, alloy disorder, and/or surface roughness. The dephasing strength is quantified by the parameter D_0. We include the effect of dephasing in a phenomenological manner by varying the dephasing strength D_0 (Appendix A 1). It can be inferred from Fig. 9 that the microwave power output remains nearly the same, while the power spectrum deteriorates with increasing dephasing strength. This phenomenon can be understood by noticing a small increase in the charge current in the noncollinear configuration of ferromagnets due to partial off resonance [17] and a reduction in the spin current (Fig. 13). We show in Fig. 10(a) the frequency of oscillation in the presence of dephasing. The frequency of oscillation also decreases in the presence of dephasing due to a reduction in the spin current. Figure 10(b) shows the variation of the FWHM with voltage in the presence of dephasing.

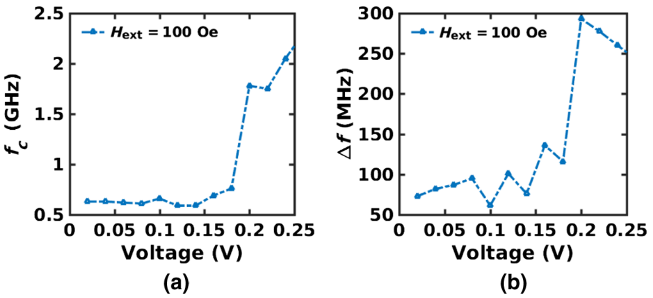

FIG. 10. (a) Voltage dependence of peak frequency. (b) FWHM Δf as a function of the bias voltage in the presence of dephasing with a strength $D_0 = 0.02$ eV^2.

IV. CONCLUSIONS

In this work, we propose and explore designs of STNOs based on resonant tunneling to harvest two of its special features, i.e., its ultrahigh TMR and its capability of exhibiting large spin currents at small bias voltages. We demonstrate that resonant spin filtering of the RTMTJ makes it the most suitable candidate for next-generation STNOs from a device perspective. We estimate that STNOs based on the RTMTJ devices deliver 1150% higher microwave power with 1100% higher efficiency than trilayer-MTJ-based oscillators. We also analyze the robustness of our STNO designs with respect to small thickness fluctuations of the quantum-well region as well as the dephasing process. We believe that the viable device designs presented here will open up alternative frontiers for experimental considerations of pentalayer structures and theoretical investigations of spin feedback oscillators [25,26] based on such structures. The RTMTJ based oscillators can pave the way for next-generation STNOs for modern communications [8].

ACKNOWLEDGMENTS

A. S. would like to acknowledge Smarika Kulshrestha for the insightful discussions. This work was supported in part by the IIT Bombay SEED grant and the Department of Science and Technology (DST), India, under Science and Engineering Board Grant No. SERB/F/3370/2013-2014.

APPENDIX A: THEORETICAL FORMULATION

We sketch the essential details of the NEGF simulation procedure [20,27–30] that was used to analyze the nano-oscillator device designs, based on the device structures detailed in Fig. 11. The trilayer MTJ has a layer of MgO between the magnets, while the RTMTJ has a heterostructure of MgO-Zn$_{1-x}$Mg$_x$O-MgO sandwiched between the fixed and free magnets, leading to resonant peaks in the transmission spectrum. The magnetization of the fixed layer is along the $\hat{z}$ axis, and that of the free layer changes with an applied bias and magnetic field.

The NEGF spin-transport formalism self-consistently coupled with the stochastic LLGS and Poisson's equations within the effective-mass framework is employed to calculate the charge and spin currents in the devices [20,27,29–31], as shown in Fig. 12. We start with an energy-resolved, spin-dependent, single-particle Green's-function matrix $[G(E)]$ evaluated from the device Hamiltonian matrix $[H]$ given by

$$[G(E)] = [EI - H - \Sigma]^{-1}, \tag{A1}$$

$$[\Sigma] = [\Sigma_T] + [\Sigma_B], \tag{A2}$$

where the device Hamiltonian matrix, $[H] = [H_0] + [U]$, comprises the device tight-binding matrix, $[H_0]$, and the

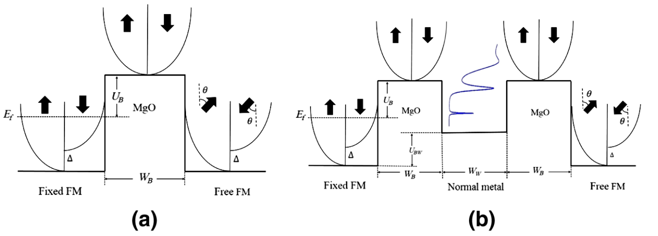

FIG. 11. Energy band schematic. (a) A trilayer MTJ device at equilibrium along the $\hat{y}$ direction. The ferromagnetic contacts have an exchange energy of Δ, with E_f being the Fermi energy and U_B the barrier height in MgO above the Fermi energy. (b) A RTMTJ device at equilibrium along the $\hat{y}$ direction. Here, U_{BW} is the difference between the bottom of the conduction band of the ferromagnet and the normal metal or semiconductor.

Coulomb charging matrix, $[U]$, in real space, and $[I]$ is the identity matrix with the dimensionality of the device Hamiltonian. The quantities $[\Sigma_T]$ and $[\Sigma_B]$ represent the self-energy matrices [31] of the top and bottom magnetic layers evaluated within the tight-binding framework [27,28]. A typical matrix representation of any quantity $[A]$ defined above entails the use of the matrix element $A(y, y', k_z, k_z', k_x, k_x', E)$, indexed on the real space y and the transverse-mode space k_z, k_x. To account for the finite cross section, we follow the uncoupled-transverse-mode approach, with each transverse mode indexed as k_z, k_x evaluated by solving the subband eigenvalue problem [28,29,32].

The charging matrix, $[U]$, is obtained via a self-consistent calculation with Poisson's equation along the transport direction $\hat{y}$ given by

$$\frac{d}{dy}\left(\epsilon_r(y)\frac{d}{dy}U(y)\right) = \frac{-q^2}{\epsilon_0}n(y), \tag{A3}$$

$$n(y) = \frac{1}{Aa_0}\sum_{k_z,k_x} G^n(y; k_z, k_x), \tag{A4}$$

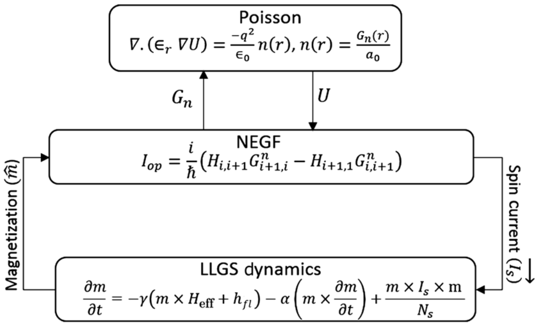

FIG. 12. Simulation engine for a nonequilibrium Green's-function spin-transport formalism self-consistently coupled to the stochastic Landau-Lifshitz-Gilbert-Slonczewski and Poisson's equations.

with $G^n(y; k_z, k_x) = G^n(y, y, k_z, k_z, k_x, k_x)$ being a diagonal element of the energy-resolved electron-correlation matrix $[G^n(E)]$ given by

$$[G^n] = \int dE[G(E)][\Sigma^{\mathrm{in}}(E)][G(E)]^{\dagger}, \tag{A5}$$

$$[\Sigma^{\mathrm{in}}(E)] = [\Gamma_T(E)]f_T(E) + [\Gamma_B(E)]f_B(E), \tag{A6}$$

Here, $[\Gamma_T(E)] = i([\Sigma_T(E)] - [\Sigma_T(E)]^{\dagger})$ and $[\Gamma_B(E)] = i([\Sigma_B(E)] - [\Sigma_B(E)]^{\dagger})$ are the spin-dependent broadening matrices [31] of the top and bottom contacts. The Fermi-Dirac distributions of the top and bottom contacts are given by $f_T(E)$ and $f_B(E)$, respectively. Here, $U(z)$ is the potential profile inside the device subject to the boundary conditions; $U_{\mathrm{fixed\,FM}} = -qV/2$ and $U_{\mathrm{free\,FM}} = qV/2$, with V being the applied voltage; A is the cross-section area of the device; a_0 is the interatomic spacing in effective-mass framework; and $\hbar$ is the reduced Planck's constant.

The summit of the calculation is the evaluation of charge currents following the self-consistent convergence of Eqs. (A3) and (A4). The matrix element of the charge current operator $\hat{I}_{\mathrm{op}}$ representing the charge current between two lattice points i and $i+1$ is given by [17]

$$I_{\mathrm{op},i,i+1} = \frac{i}{\hbar}(H_{i,i+1}G^n_{i+1,i} - G^{n\dagger}_{i,i+1}H^{\dagger}_{i+1,i}), \tag{A7}$$

following which the charge current I and spin current I_S are given by $I = q\int dE\mathrm{Real}[\mathrm{Trace}(\hat{I}_{\mathrm{op}})]$, $I_{S\sigma} = q\int dE\mathrm{Real} \times [\mathrm{Trace}(\sigma_S \cdot \hat{I}_{\mathrm{op}})]$, respectively, where the current operator $\hat{I}_{\mathrm{op}}$ is a 2×2 matrix in spin space, H is the Hamiltonian matrix of the system, and q is the electronic charge.

We resolve the spin current as $\vec{I_S} = I_{S,m}\hat{m} + I_{S,\parallel}\hat{M} + I_{S,\perp}\hat{M} \times \hat{m}$. The $I_{S\parallel}$ value along $\hat{M}$ is known as the Slonczewski spin-transfer-torque term and the $I_{S\perp}$ value along $\hat{M} \times \hat{m}$ is known as the fieldlike term. We use the LLGS equation to calculate the magnetization dynamics of the free layer in the presence of an applied magnetic field and spin current [15,33]:

$$\begin{aligned}(1+\alpha^2)\frac{\partial \hat{m}}{\partial t} &= -\gamma\hat{m} \times (\vec{H}_{\mathrm{eff}} + \vec{h_{\mathrm{fl}}}) \\ &\quad - \gamma\alpha\{\hat{m} \times [\hat{m} \times (\vec{H}_{\mathrm{eff}} + \vec{h_{\mathrm{fl}}})]\} \\ &\quad - \frac{\gamma\hbar}{2qM_S V}\{[\hat{m} \times (\hat{m} \times \vec{I_S})] - \alpha(\hat{m} \times \vec{I_S})\},\end{aligned}$$

where $\hat{m}$ is the unit vector along the direction of magnetization of the free magnet, γ is the gyromagnetic ratio of the electron, and α is the Gilbert-damping parameter. $\vec{H}_{\mathrm{eff}} = \vec{H}_{\mathrm{app}} + H_k m_z\hat{z} - H_d m_x\hat{x}$ is the effective magnetic field, with $\vec{H}_{\mathrm{app}}$ being the applied external field, $H_k = (2K_{u\parallel}/M_S)$ being the anisotropy field, and $H_d = 4\pi N_x M_s - (2K_{u\perp}/M_S)$ being the effective demagnetization field. N_x

is the demagnetization factor [34,35], $K_{u\parallel}$ and $K_{u\perp}$ are in-plane and perpendicular uniaxial anisotropy constants, respectively, M_S is the saturation magnetization of the free layer, and V is the volume of the free ferromagnetic layer. In this work, we also take into account the thermal noise in the form of magnetic-field fluctuations $\vec{h_r}$ in the LLGS equation with the following statistical properties [18]:

$$\langle h_{\mathrm{fl,i}}(t)\rangle = 0, \langle h_{\mathrm{fl},i} h_{\mathrm{fl},j}(s)\rangle = 2D\delta_{ij}\delta(t-s), \quad \text{(A8)}$$

where i and j are Cartesian indices and $\langle\cdots\rangle$ represents the ensemble average. The strength of the fluctuation D is given by

$$D = \frac{\alpha}{1+\alpha^2}\frac{k_B T}{\gamma\mu_0 M_S V}, \quad \text{(A9)}$$

where μ_0 is the free-space permeability constant, k_B is the Boltzmann constant, and T is the temperature of the magnetic layer.

1. Elastic dephasing

In the presence of dephasing, Eqs. (A2) and (A6) are modified as

$$[\Sigma(E)] = [\Sigma_T(E)] + [\Sigma_B(E)] + [\Sigma_0(E)], \quad \text{(A10)}$$

$$[\Sigma^{\mathrm{in}}(E)] = [\Gamma_T(E)]f_T(E) + [\Gamma_B(E)]f_B(E) + [\Sigma_0^{\mathrm{in}}(E)]. \quad \text{(A11)}$$

For dephasing processes, $\Sigma_0(E)$ and $\Sigma_0^{\mathrm{in}}(E)$ are given by

$$[\Sigma_0(E)] = D \times [G(E)], \quad \text{(A12)}$$

$$[\Sigma_0^{\mathrm{in}}(E)] = D \times [G^n(E)], \quad \text{(A13)}$$

where × denotes element-by-element multiplication. The matrix elements of $[D]$ denote the correlation function of the random potential due to impurities [17,36].

In our simulations, we account for the dephasing which destroys momentum and phase with $D_{ij} = D_0$ for $i = j$ and $D_{ij} = 0$ for $i \neq j$ by a self-consistent solution of Eqs. (A1), (A10), (A5), and (A11). The magnitude of D_0 signifies the strength of the dephasing.

In Figs. 13(a) and 13(b), we show the effect of dephasing on the transmission peak in the PC of ferromagnets and the I-V characteristics of the RTMTJ device in the perpendicular configuration of ferromagnets, respectively. We show in Fig. 13(c) the effect of dephasing on the angular dependence of the charge current. In the noncollinear configuration of the ferromagnets, there is an increase in the charge current in the presence of dephasing due to a partial off-resonance conduction. It can be inferred from Table I that, in the PC, the percentage reduction in the charge current (0.7%) with dephasing is smaller than the percentage increase in the charge current (3.4%), with dephasing in the APC due to off resonance [17]. Thus, dephasing reduces the TMR of the RTMTJ device, as shown in Table I. The Slonczewski ($I_{S\parallel}$) spin current also decreases with dephasing due to phase relaxation, as depicted in Fig. 13(d). It is interesting to note, from Table I, that the spin current is more sensitive to dephasing than the TMR of the RTMTJ device. We also believe that a more detailed study of elastic and inelastic scattering in the RTMTJ structure may lead to some interesting physics, especially in the nonlinear configuration of the ferromagnets, which will be discussed in an upcoming work.

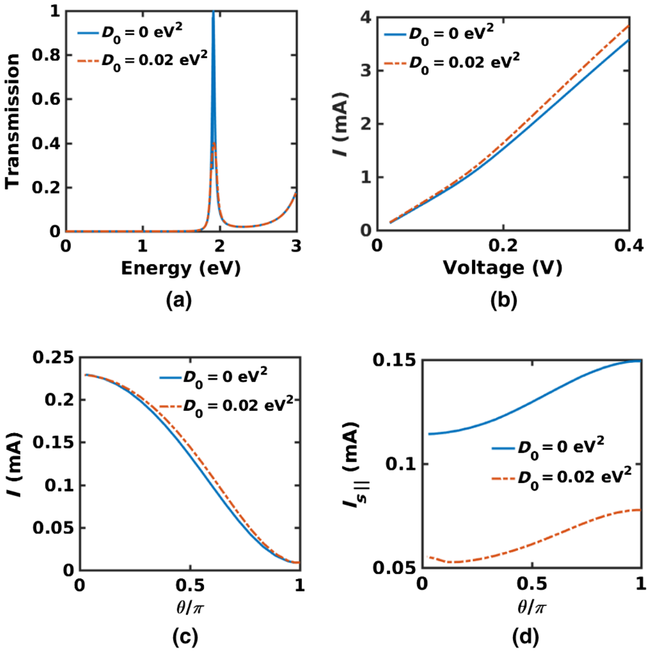

FIG. 13. (a) Transmission spectrum for up-spin electrons in the presence of dephasing for the lowest-order transverse mode. (b) I-V characteristics in the presence of dephasing in the perpendicular configuration of the ferromagnets. The effect of dephasing on the angular dependence of (c) the charge current and (d) $I_{S\parallel}$ (the Slonczewski term) at $V = 20$ mV is shown.

2. Numerical-simulation details

We now outline the details of the numerical simulation. We use the effective-mass Hamiltonian to describe the

TABLE I. Effect of dephasing on a RTMTJ device at $V = 20$ mV.

D_0 (eV^2)	T-peak % reduction	I_{PC} (mA)	I_{APC} (mA)	TMR (%)	$I_{s\parallel}$ (mA) $\theta = \pi/2$
0	0	0.2296	0.0088	2509	0.1297
0.0025	25	0.2293	0.0089	2482	0.0103
0.0050	40	0.2280	0.0089	2453	0.0888
0.0200	60	0.2280	0.0091	2416	0.0612

RTMTJ heterostructure within the tight-binding formalism along the direction of transport. The well region consists of stoichiometrically substituted ZnO with Mg $(\mathrm{Zn}_{1-x}\mathrm{Mg}_x\mathrm{O})$, whose band gap and work function may be tuned; the presented device design has a stoichiometric fraction of Mg, $x = 0.43$. The effective mass and band offset of the well region (U_{BW}) is obtained by linear interpolation between the effective masses and the band offsets of MgO and ZnO, weighted appropriately by a stoichiometric fraction of Mg. The effective mass of MgO is $m_{OX} = 0.16 m_e$ [28] and of ZnO is $m_{\mathrm{ZnO}} = 0.29 m_e$ [19], with m_e being the free-electron mass [28,37,38]. The band offset between MgO and ZnO is $U_{BW} = -0.51$ eV [19]. We use (Co,Fe)B as a ferromagnet, with the Fermi energy $E_f = 2.25$ eV, exchange splitting $\Delta = 2.15$ eV, and effective mass $m_{\mathrm{FM}} = 0.38 m_e$ [28,38]. The barrier height of the (Co,Fe)B-MgO interface is $U_B = 0.76$ eV above the Fermi energy [28,37]. The thickness of the barrier region and the well region is $W_B = 0.8$ nm and $W_W = 1$ nm, respectively. The RTMTJ may also be realized by a heterostructure of MgO either with Ge [39] or with a stoichiometrically substituted MgO $(\mathrm{Mg}_x\mathrm{Zn}_{1-x}\mathrm{O})$ with Zn, whose band gap and work function may be tailored [40]. We discretize the effective-mass Hamiltonian with a lattice constant of $a = 0.25$ Å such that a further reduction in the lattice constant does not affect the results significantly. This approach to discretizing the effective-mass Hamiltonian and recasting it in the tight-binding formalism was used extensively in many previous works [12,20,27–30,38].

We show in Fig. 12 the simulation engine to solve the coupled dynamics of the ferromagnet and spin transport. Although the simulation engine seems to be computationally very heavy, the simulation time can be significantly reduced by making an observation that the self-consistent solution of the NEGF with Poisson's equation needs to be done only once at a particular voltage for different relative orientations between the fixed and free ferromagnets. The Poisson potential across the structure remains nearly the same for different angles between the fixed and free ferromagnets at a particular bias voltage, which reduces the simulation time by a considerable amount.

We recast the LLGS equation in the Langevin form to take into account Gaussian stochastic processes to solve the Fokker-Planck equation. We use the numerical Heun scheme to correctly solve the stochastic magnetization dynamics as pointed by García-Palacios and Lázaro [18]. We take the integration step of the stochastic LLGS equation as 1 psec. To determine the central frequency of oscillation and the FWHM, we simulate the magnetization dynamics for 0.1 μsec and take the ensemble average of the signal's fast Fourier transform over 1000 samples. On the other hand, the microwave power is calculated using Eq. (3), which eliminates the need for longtime magnetization-dynamics simulations.

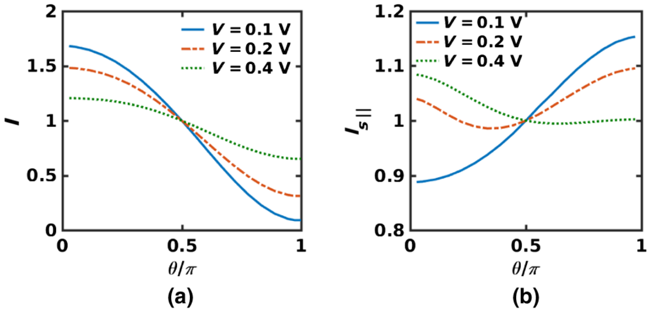

FIG. 14. Angular dependence of (a) charge current and (b) $I_{S\|}$ (the Slonczewski term). The currents at the two different voltages are normalized to their values at perpendicular configurations of the fixed and free ferromagnetic layers.

3. Angular dependence of the current

Figure 14(a) shows the variation of the charge current with azimuthal angle between fixed and free ferromagnets. We show in Fig. 14(b) the angular dependence of $I_{S\|}$ (the Slonczewski term) at different voltages. The angular dependence of the spin current varies with voltage and significantly deviates from that of the trilayer-MTJ device [32] and a double-barrier structure with a ferromagnet in the quantum-well region [41].

APPENDIX B: MAGNETIZATION DYNAMICS

We show in Fig. 15 the magnetization dynamics of the trilayer device under different applied biases. It can be seen in Fig. 15 that, as the bias voltage increases, the out-of-plane component of the magnetization increases (m_y) due to the large spin current, which results in a high frequency of oscillations. Also, it can be seen from Fig. 15 that the

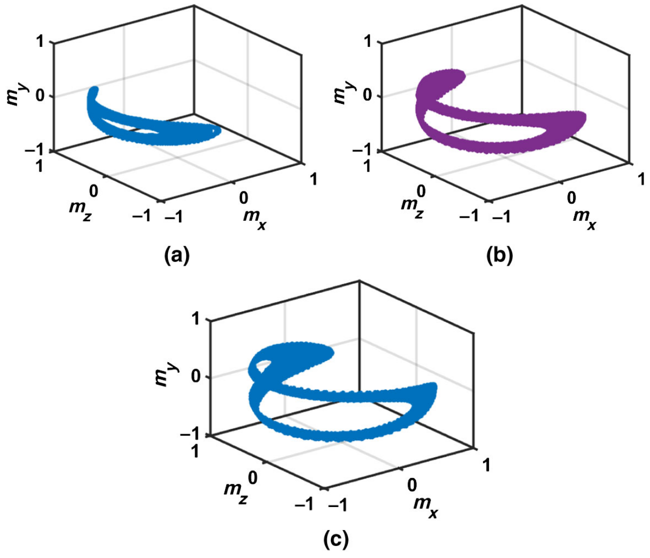

FIG. 15. Magnetization dynamics of the trilayer-MTJ device with (a) an applied bias of $V = 0.10$ V, (b) $V = 0.14$ V, and (c) $V = 0.16$ V, and an applied magnetic field of 100 Oe.

spread in the magnetization dynamics due to thermal noise reduces with the bias voltage, resulting in small linewidths of oscillations.

[1] Vasil Tiberkevich, Andrei Slavin, and Joo-Von Kim, Microwave power generated by a spin-torque oscillator in the presence of noise, Appl. Phys. Lett. **91**, 192506 (2007).

[2] Joo-Von Kim, Stochastic theory of spin-transfer oscillator linewidths, Phys. Rev. B **73**, 174412 (2006).

[3] Joo-Von Kim, Vasil Tiberkevich, and Andrei N. Slavin, Generation Linewidth of an Auto-oscillator with a Nonlinear Frequency Shift: Spin-Torque Nano-oscillator, Phys. Rev. Lett. **100**, 017207 (2008).

[4] A. Slavin and V. Tiberkevich, Nonlinear auto-oscillator theory of microwave generation by spin-polarized current, IEEE Trans. Magn. **45**, 1875 (2009).

[5] Joo Von Kim, in *Solid State Physics*, Vol. 63, 1st ed., edited by Robert L. Stamps and Robert E. Camley (Elsevier, New York, 2012), p. 217.

[6] J. A. Katine and Eric E. Fullerton, Device implications of spin-transfer torques, J. Magn. Magn. Mater. **320**, 1217 (2008).

[7] S. A. Wolf, A. Y. Chtchelkanova, and D. M. Treger, Spintronics 2014: A retrospective and perspective, IBM J. Res. Dev. **50**, 101 (2006).

[8] Hyun Seok Choi, Sun Yool Kang, Seong Jun Cho, Inn-Yeal Oh, Mincheol Shin, Hyuncheol Park, Chaun Jang, Byoung-Chul Min, Sang-Il Kim, Seung-Young Park, and Chul Soon Park, Spin nano-oscillator-based wireless communication, Sci. Rep. **4**, 5486 (2014).

[9] M. Covington, M. AlHajDarwish, Y. Ding, N. J. Gokemeijer, and M. A. Seigler, Current-induced magnetization dynamics in current perpendicular to the plane spin valves, Phys. Rev. B **69**, 184406 (2004).

[10] Alina M. Deac, Akio Fukushima, Hitoshi Kubota, Hiroki Maehara, Yoshishige Suzuki, Shinji Yuasa, Yoshinori Nagamine, Koji Tsunekawa, David D. Djayaprawira, and Naoki Watanabe, Bias-driven large power microwave emission from MgO-based tunnel magnetoresistance devices, Nat. Phys. **4**, 803 (2008).

[11] Zhongming Zeng, Pedram Khalili Amiri, Ilya N. Krivorotov, Hui Zhao, Giovanni Finocchio, Jian-Ping Wang, Jordan A. Katine, Yiming Huai, Juergen Langer, Kosmas Galatsis, Kang L. Wang, and HongWen Jiang, High-power coherent microwave emission from magnetic tunnel junction nano-oscillators with perpendicular anisotropy, ACS Nano **6**, 6115 (2012).

[12] Niladri Chatterji, Ashwin A. Tulapurkar, and Bhaskaran Muralidharan, Enhancement of spin-transfer torque switching via resonant tunneling, Appl. Phys. Lett. **105**, 232410 (2014).

[13] Abhishek Sharma, Ashwin Tulapurkar, and Bhaskaran Muralidharan, Ultrasensitive nanoscale magnetic-field sensors based on resonant spin filtering, IEEE Trans. Electron Devices **63**, 4527 (2016).

[14] L. Berger, Emission of spin waves by a magnetic multilayer traversed by a current, Phys. Rev. B **54**, 9353 (1996).

[15] J. C. Slonczewski, Current-driven excitation of magnetic multilayers, J. Magn. Magn. Mater. **159**, L1 (1996).

[16] P.-Y. Clment, C. Baraduc, C. Ducruet, L. Vila, M. Chshiev, and B. Diny, Modulation of spin transfer torque amplitude in double barrier magnetic tunnel junctions, Appl. Phys. Lett. **107**, 102405 (2015).

[17] Supriyo Datta, *Electronic Transport in Mesoscopic Systems* (Cambridge University Press, Cambridge, England, 1997).

[18] José Luis García-Palacios and Francisco J. Lázaro, Langevin-dynamics study of the dynamical properties of small magnetic particles, Phys. Rev. B **58**, 14937 (1998).

[19] K. Shi, P. F. Zhang, H. Y. Wei, C. M. Jiao, C. M. Li, X. L. Liu, S. Y. Yang, Q. S. Zhu, and Z. G. Wang, Energy band alignment of MgO $(111)/$ZnO (0002) heterojunction determined by x-ray photoelectron spectroscopy, Solid State Commun. **152**, 938 (2012).

[20] Ioannis Theodonis, Nicholas Kioussis, Alan Kalitsov, Mairbek Chshiev, and W. H. Butler, Anomalous Bias Dependence of Spin Torque in Magnetic Tunnel Junctions, Phys. Rev. Lett. **97**, 237205 (2006).

[21] D. Houssameddine, U. Ebels, B. Delaët, B. Rodmacq, I. Firastrau, F. Ponthenier, M. Brunet, C. Thirion, J.-P. Michel, L. Prejbeanu-Buda, M.-C. Cyrille, O. Redon, and B. Dieny, Spin-torque oscillator using a perpendicular polarizer and a planar free layer, Nat. Mater. **6**, 447 (2007).

[22] A. G. Petukhov, A. N. Chantis, and D. O. Demchenko, Resonant Enhancement of Tunneling Magnetoresistance in Double-Barrier Magnetic Heterostructures, Phys. Rev. Lett. **89**, 107205 (2002).

[23] C. H. Chen and W. J. Hsueh, Enhancement of tunnel magnetoresistance in magnetic tunnel junction by a superlattice barrier, Appl. Phys. Lett. **104**, 042405 (2014).

[24] M. Chshiev, D. Stoeffler, A. Vedyayev, and K. Ounadjela, Magnetic diode effect in double-barrier tunnel junctions, Europhys. Lett. **58**, 257 (2002).

[25] Dinesh Kumar, K. Konishi, Nikhil Kumar, S. Miwa, A. Fukushima, K. Yakushiji, S. Yuasa, H. Kubota, C. V. Tomy, A. Prabhakar, Y. Suzuki, and A. Tulapurkar, Coherent microwave generation by spintronic feedback oscillator, Sci. Rep. **6**, 30747 (2016).

[26] Swapnil Bhuktare, Hanuman Singh, Arnab Bose, and Ashwin. A. Tulapurkar, Spintronic Oscillator Based on Spin-Current Feedback Using the Spin Hall Effect, Phys. Rev. Applied **7**, 014022 (2017).

[27] Ahmet Ali Yanik, Gerhard Klimeck, and Supriyo Datta, Quantum transport with spin dephasing: A nonequlibrium Green's function approach, Phys. Rev. B **76**, 045213 (2007).

[28] D. Datta, B. Behin-Aein, Supriyo Datta, and Sayeef Salahuddin, Voltage asymmetry of spin-transfer torques, IEEE Trans. Nanotechnol. **11**, 261 (2012).

[29] M. P. Anantram, Mark S. Lundstrom, and Dmitri E. Nikonov, Modeling of nanoscale devices, Proc. IEEE **96**, 1511 (2008).

[30] Akshay Agarwal and Bhaskaran Muralidharan, Power and efficiency analysis of a realistic resonant tunneling diode thermoelectric, Appl. Phys. Lett. **105**, 013104 (2014).

[31] Supriyo Datta, *Quantum Transport: Atom to Transistor* (Cambridge University Press, Cambridge, England, 2005).

[32] Sayeef Salahuddin, Deepanjan Datta, Prabhakar Srivastava, and Supriyo Datta, in *Proceedings of the 2007 IEEE*

International Electron Devices Meeting, Washington, DC, 2007 (IEEE, New York, 2008), p. 121.

[33] Arne Brataas, Andrew D. Kent, and Hideo Ohno, Current-induced torques in magnetic materials, Nat. Mater. **11**, 372 (2012).

[34] Sören Boyn, João Sampaio, Vincent Cros, Julie Grollier, Akio Fukushima, Hitoshi Kubota, Kay Yakushiji, and Shinji Yuasa, Twist in the bias dependence of spin torques in magnetic tunnel junctions, Phys. Rev. B **93**, 224427 (2016).

[35] J. A. Osborn, Demagnetizing factors of the general ellipsoid, Phys. Rev. **67**, 351 (1945).

[36] Roksana Golizadeh-Mojarad and Supriyo Datta, Nonequilibrium Green's function based models for dephasing in quantum transport, Phys. Rev. B **75**, 081301 (2007).

[37] Hitoshi Kubota, Akio Fukushima, Kay Yakushiji, Taro Nagahama, Shinji Yuasa, Koji Ando, Hiroki Maehara, Yoshinori Nagamine, Koji Tsunekawa, David D. Djayaprawira, Naoki Watanabe, and Yoshishige Suzuki, Quantitative measurement of voltage dependence of spin-transfer torque in MgO-based magnetic tunnel junctions, Nat. Phys. **4**, 37 (2007).

[38] Deepanjan Datta, Ph.D. thesis, Purdue University, 2012.

[39] D. Petti, M. Cantoni, C. Rinaldi, and R. Bertacco, Chemical and electronic properties of Fe/MgO/Ge heterostructures for spin electronics, J. Phys. Conf. Ser. **292**, 012010 (2011).

[40] D. L. Li, Q. L. Ma, S. G. Wang, R. C. C. Ward, T. Hesjedal, X.-G. Zhang, A. Kohn, E. Amsellem, G. Yang, J. L. Liu, J. Jiang, H. X. Wei, and X. F. Han, Controlling spin-dependent tunneling by bandgap tuning in epitaxial rocksalt MgZnO films, Sci. Rep. **4**, 7277 (2014).

[41] Ioannis Theodonis, Alan Kalitsov, and Nicholas Kioussis, Enhancing spin-transfer torque through the proximity of quantum well states, Phys. Rev. B **76**, 224406 (2007).